Supporting Information

Fast Organic Cation-exchange in Colloidal Perovskite Quantum Dots towards Functional Optoelectronic Applications

Chenyu Zhao,[1,2] Claudio Cazorla,[3] Xuliang Zhang,[1,2] Hehe Huang,[1,2] Xinyu Zhao,[1,2] Du Li,[1,2] Junwei Shi,[1] Qian Zhao,[5] Wanli Ma,[1,4] Jianyu Yuan[1,2]*

[1]Institute of Functional Nano & Soft Materials (FUNSOM), Soochow University, Suzhou, Jiangsu 215123, P. R. China
[2]Jiangsu Key Laboratory of Advanced Negative Carbon Technologies, Soochow University, Suzhou, 215123, Jiangsu, P. R. China
[3]Departament de Física, Universitat Politècnica de Catalunya Campus Nord B4–B5, 08034 Barcelona (Spain)
[4]Jiangsu Key Laboratory for Carbon-Based Functional Materials and Devices, Soochow University, Suzhou, Jiangsu 215123, P. R. China
[5]School of Materials Science and Engineering, Nankai University, Tianjin 300350, P. R. China
*To whom correspondence should be addressed. E-mail: jyyuan@suda.edu.cn

1. Characterizations

The UV-vis absorption spectroscopy was performed on a Perkin Elmer model Lambda 750 spectrophotometer. The PL and *in situ* PL spectra were measured by FX2000-EX (Ideaoptics) with excitation wavelength at 400 nm. The TRPL spectra were obtained using a Hamamatsu streak camera. PL data were analyzed on a Nikon 50x objective (N.A. 0.55) in a Nikon ME600 optical microscope. FTIR spectra were collected using a Bruker HYPERION FTIR spectrometer and cumulated 32 scans at a resolution of 4 cm^{-1}. The TEM images were recorded by a Tecnai G2 F20 S-Twin system operated at 200 kV. XRD patterns were performed on a desktop diffractometer (D2 PHASER, Bruker) with a Cu Kα source (λ = 1.54056 Å). The crystalline structure and crystal orientation were obtained by XRD (Rigaku D/Max-Ra X-ray diffractometer with a monochrome at Cu Kα radiation (λ ~ 1.54 Å)). The SEM images were obtained from SEM (a Zeiss G500 with the extra high tension of 10 kV). *J-V* curves of the devices carried out at a Keithley 2400 Digital Source Meter under N_2 glovebox and simulated AM 1.5G spectrum at 100 mW cm^{-2} with a solar simulator (Class AAA, 94023A-U, Newport). The external quantum efficiency (EQE) measurement of the solar cells was measured by a Solar Cell Scan 100 system (Zolix Instruments Co. Ltd.).

2. Synthesis of $CsPbI_3$, $MAPbI_3$ and $FAPbI_3$ PQDs.

$CsPbI_3$: Cs-oleate precursor was prepared by adding 2 g Cs_2CO_3, 100 mL 1-ODE and 8 mL OA into a 250 mL three-necked flask and degassing under vacuum at 90 ℃ for 1 hour. Then the mixture was heated to 120 ℃ until a clear Cs-oleate precursor was obtained for the next step. In another 250 mL flask, 1 g PbI_2, 50 mL 1-ODE, 5 mL OA and 5 mL OLA were mixed and degassed under vacuum at 90 ℃ for 2 hours and then was heated to 160 ℃ under N_2 flow. 4 mL of the Cs-oleate was injected into the PbI_2 solution and quenching the solution with ice bath after 5 s reaction.

$MAPbI_3$: MA-oleate precursor was prepared by adding 0.5 g MAAc, 5 mL ODE and 5 mL OA into a 50 mL three-necked flask and degassing under vacuum at 70 ℃ for 2 hours. Then the mixture was heated to 100 ℃ for 1 minute to remove extra water and oxygen and cooled down to 70 ℃ for the next step. In another 250 mL flask, 1 g PbI_2, 40 mL 1-ODE, 8 mL OA and 4 mL OLA were mixed and degassed under vacuum at 90 ℃ for 2 hours and then was cooled down to 70 ℃ under N_2 flow. 10 mL of the MA-oleate was injected into the PbI_2 solution and quenching the solution with ice bath after 5 s reaction.

$FAPbI_3$: FA-oleate precursor was prepared by adding 0.52 g FAAc, 10 mL OA into a 50 mL three-necked flask and degassing under vacuum at 90 ℃ for 2 hours. Then the mixture was heated to 120 ℃ for 1 minute to remove extra water and oxygen and cooled down to 80 ℃ for the next step. In another 250 mL flask, 0.688 g PbI_2, 40 mL 1-ODE, 8 mL OA and 4 mL OLA were mixed and degassed under vacuum at 90 ℃ for 2 hours and then was cooled down to 80 ℃ under N_2 flow. 10 mL of the FA-oleate was injected into the PbI_2 solution and quenching the solution with ice bath after 5 s reaction.

3. DFT calculation methods

First-principles calculations based on density functional theory (DFT)[1] were carried out with the PBEsol exchange-correlation energy functional[2] as it is implemented in the VASP software[3]. The projector-augmented wave method (PAW)[4] was employed to represent the ionic cores by considering the following electronic states as valence: Pb 6*p* 5*d* 6*s*; I 6*s* 5*p*; C 2*s* 2*p*; N 2*s* 2*p*; H 1*s*. The Grimme's D3 scheme[5] was employed for a better treatment of the dispersion interactions in the system. An energy cutoff of 750 eV and a dense Monkhorst-Pack k-point density (equal to that of a 14×14×14 grid for a 5-atom bulk cubic unit cell) were used for integrations within the Brillouin zone, leading to total energies converged to within 1 meV per atom. Atomic relaxations were concluded when the forces in the atoms were all below 0.005 eV/Å. *Ab initio* nudged-elastic band (NEB) calculations[6] were conducted to estimate

the energy barrier for molecular cation migration in bulk $MAPbI_3$, $FAPbI_3$, and $MA_{0.5}FA_{0.5}PbI_3$. In this case, we used a 4 × 4 × 4 Γ-centered k-point grid for Brillouin zone sampling and an energy cutoff of 550 eV. The geometry optimizations were halted when the forces on the atoms were all smaller than 0.01 eV/Å. The simulation cells employed in the NEB calculations contained 88 ($MAPbI_3$ and $FAPbI_3$) and 184 ($MA_{0.5}FA_{0.5}PbI_3$) atoms and a total of 8 images were interpolated between the initial and final equilibrium configuration.

4. Responsivity and detectivity calculation of photodetectors

The Responsivity of the photodetector devices were obtained from the formula:

$$R = \frac{e}{hc/\lambda} \times EQE,$$

where e is the electron charge, h is Planck's constant, c is the speed of light, and λ is the incoming wavelength.

The D* values of photodetector devices were obtained from the formula:

$$D^* = \frac{\sqrt{S * \Delta f * \mathrm{R}}}{i_n},$$

where S is the effective active area of the device, i_n is the noise current, Δf is the bandwidth (assumed to be 1 Hz)

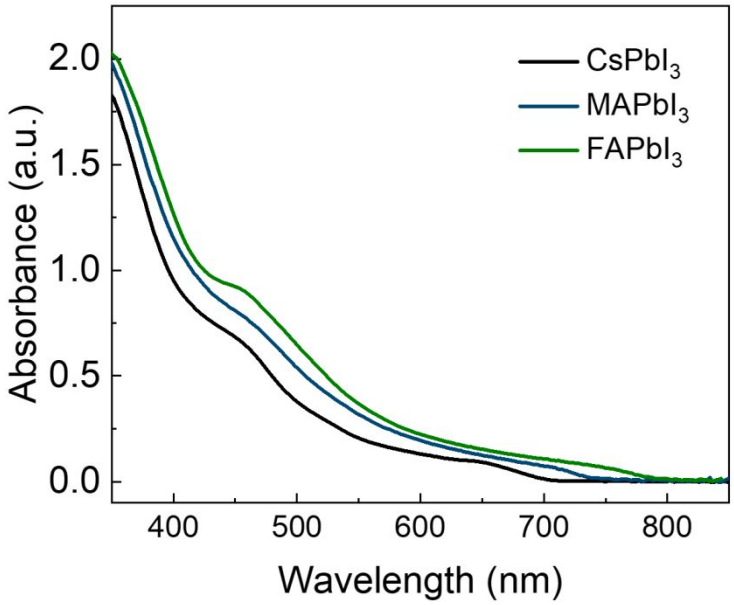

Figure S1. UV-Vis of as-synthesized $CsPbI_3$, $MAPbI_3$ and $FAPbI_3$ PQDs

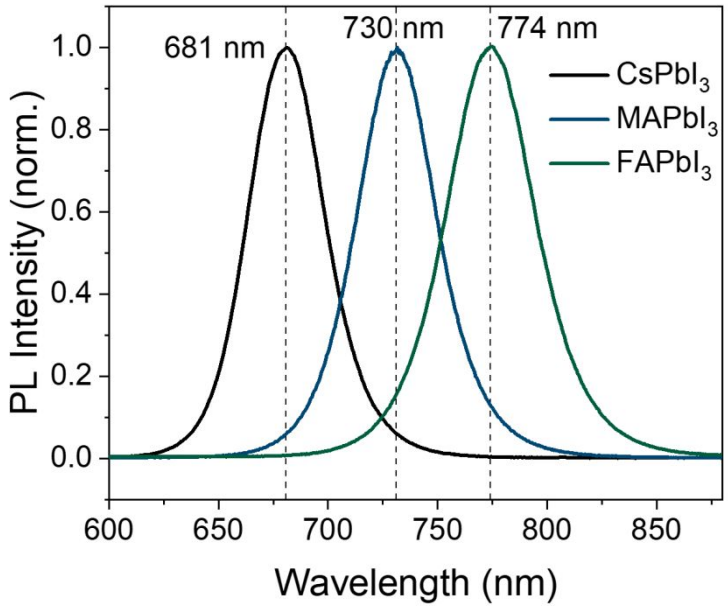

Figure S2. PL spectra of as-synthesized $CsPbI_3$, $MAPbI_3$ and $FAPbI_3$ PQDs

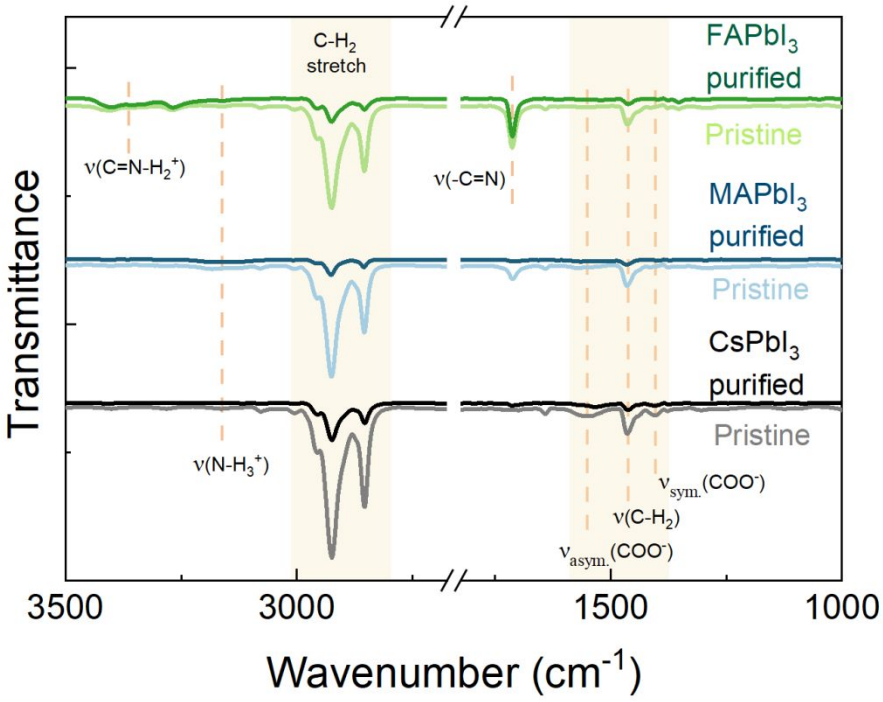

Figure S3. FTIR spectra of as-synthesized $CsPbI_3$, $MAPbI_3$ and $FAPbI_3$ PQDs before and after multiple purification process

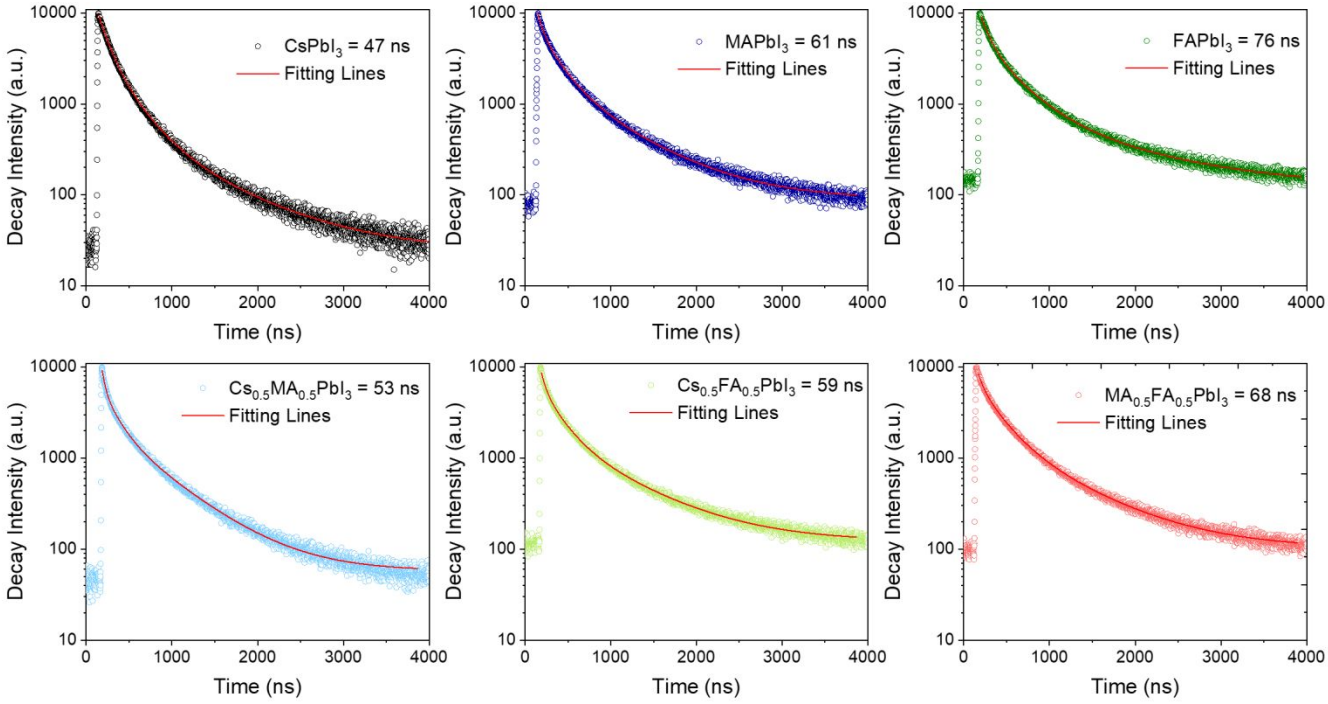

Figure S4. TRPL spectra of as-synthesized $CsPbI_3$, $MAPbI_3$ and $FAPbI_3$ PQDs

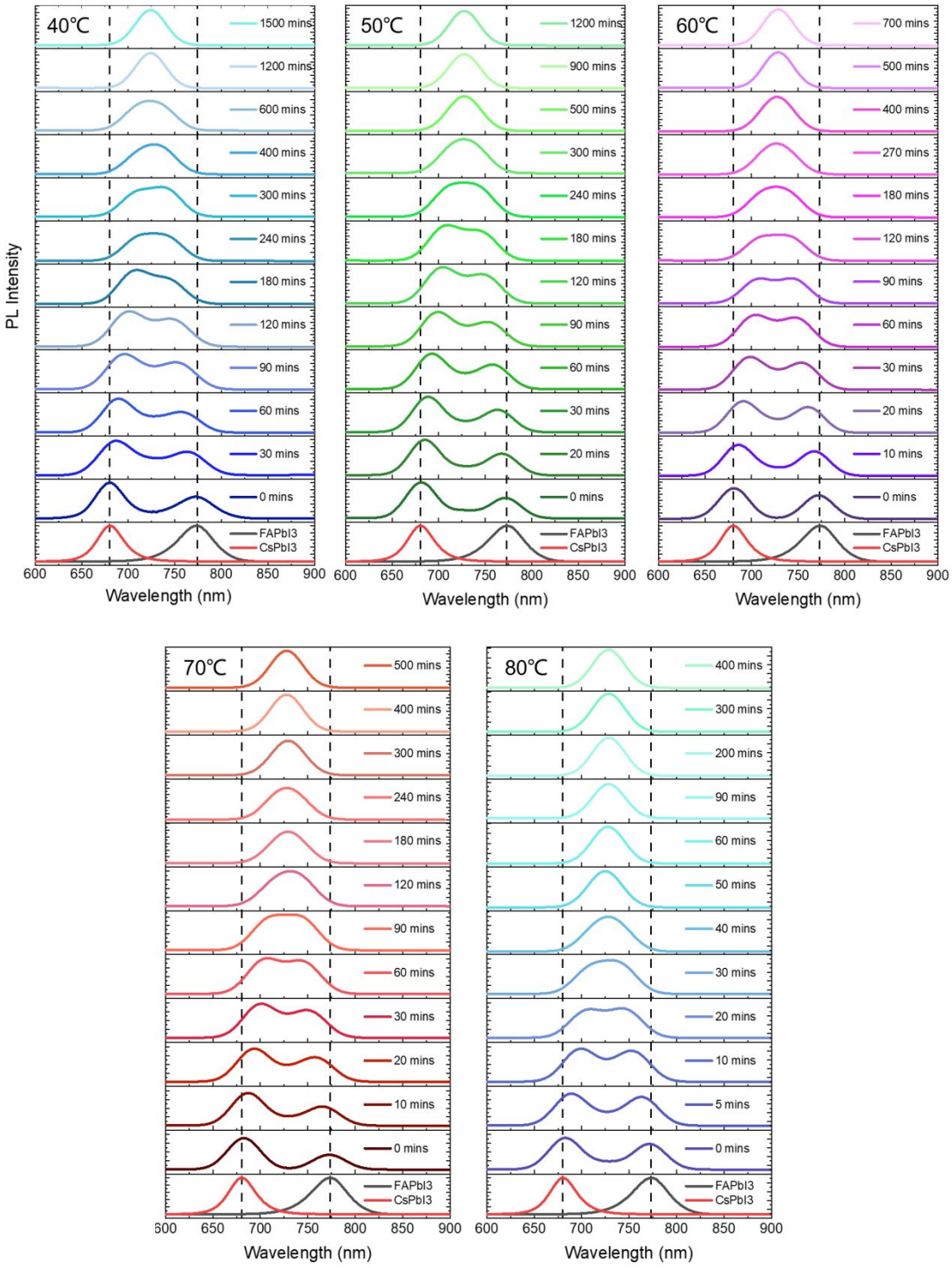

Figure S5. PL evolution of Cs^{+}-FA^{+} reaction. The data are collected at different elevated temperatures ranging from 40 °C to 80 °C

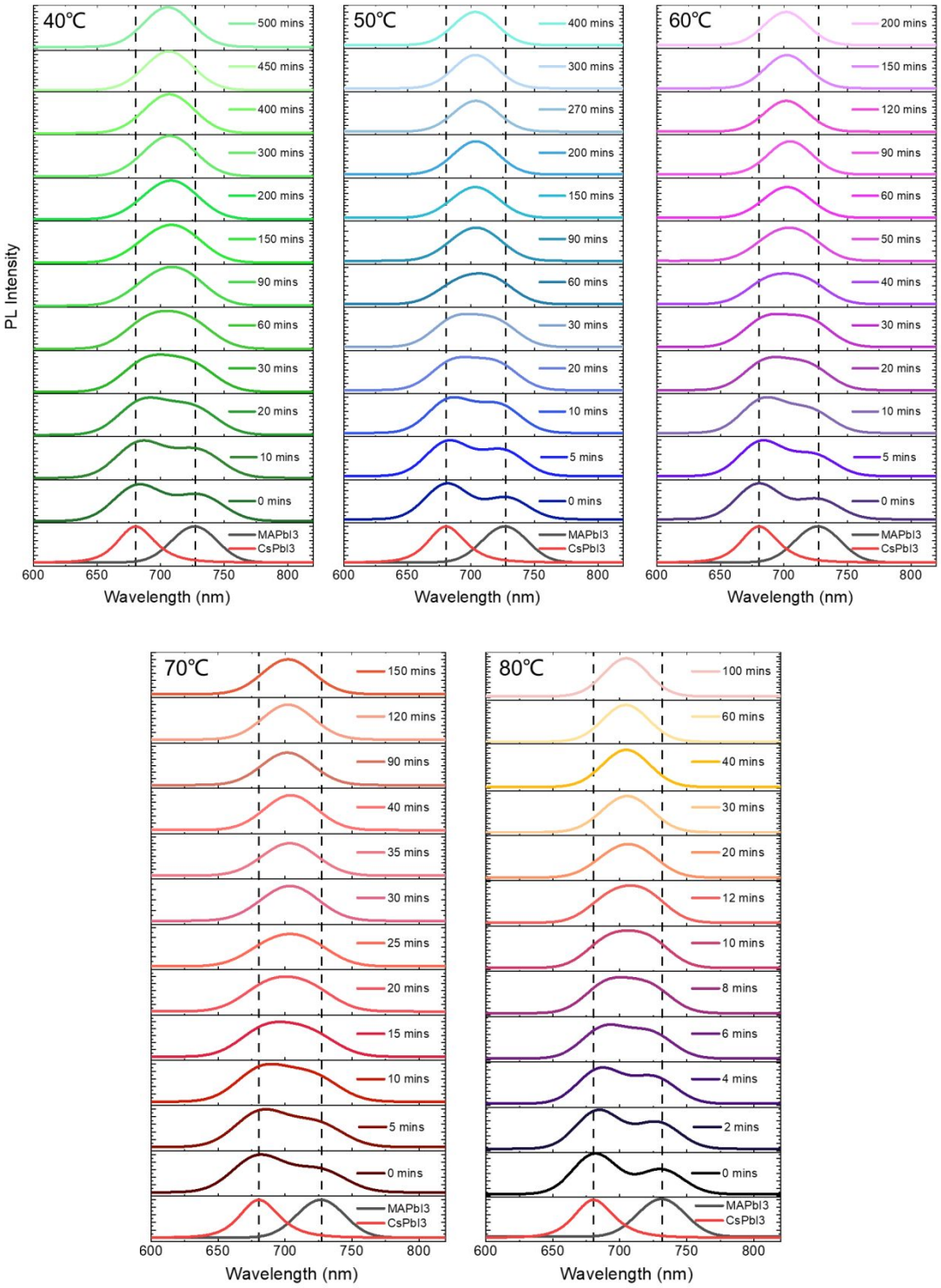

Figure S6. PL evolution of Cs^{+}-MA^{+} reaction. The data are collected at different elevated temperatures ranging from 40 °C to 80 °C

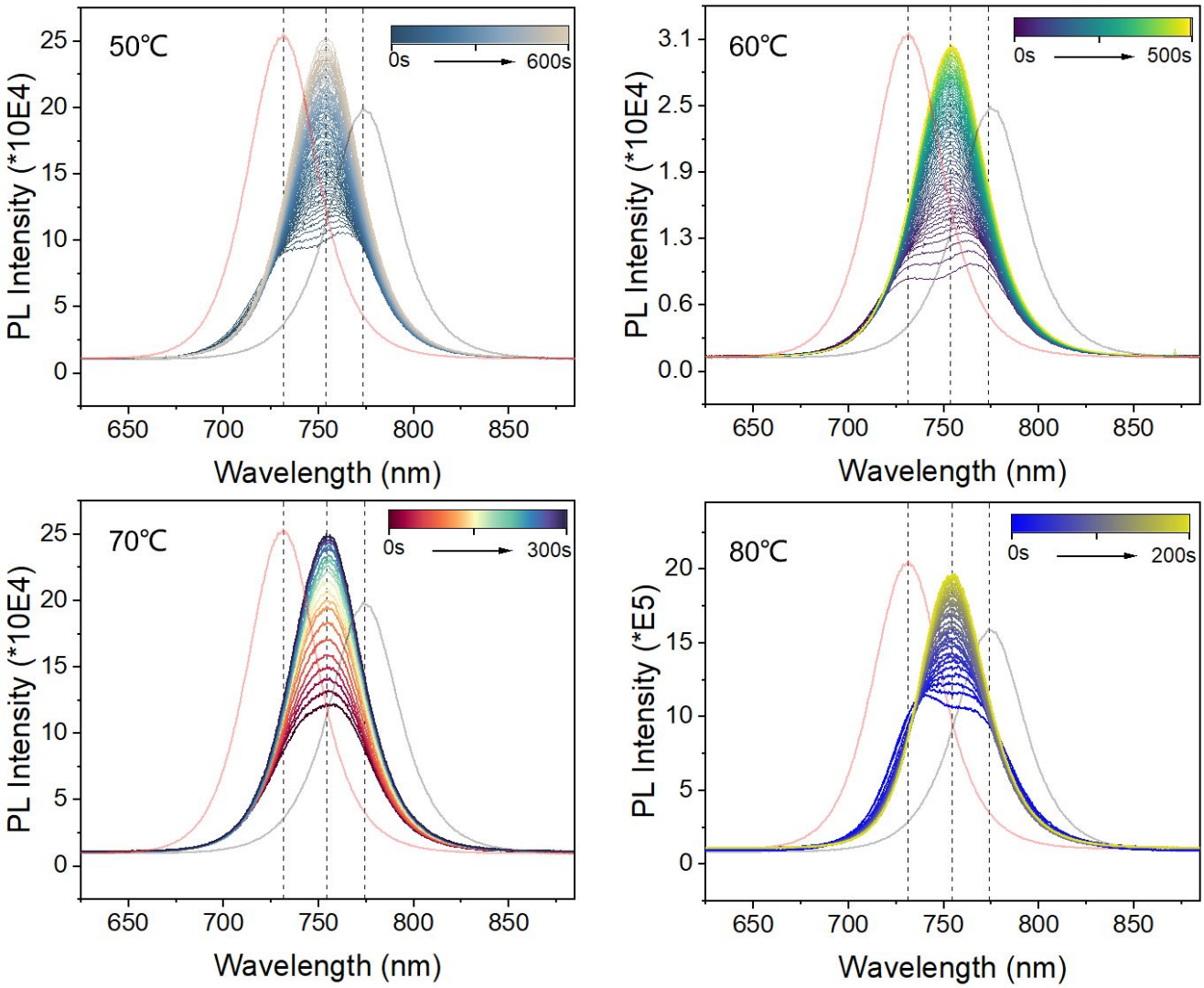

Figure S7. PL evolution of MA^+-FA^+ reaction. The data are collected at different temperatures (50°C, 60°C, 70°C, 80°C).

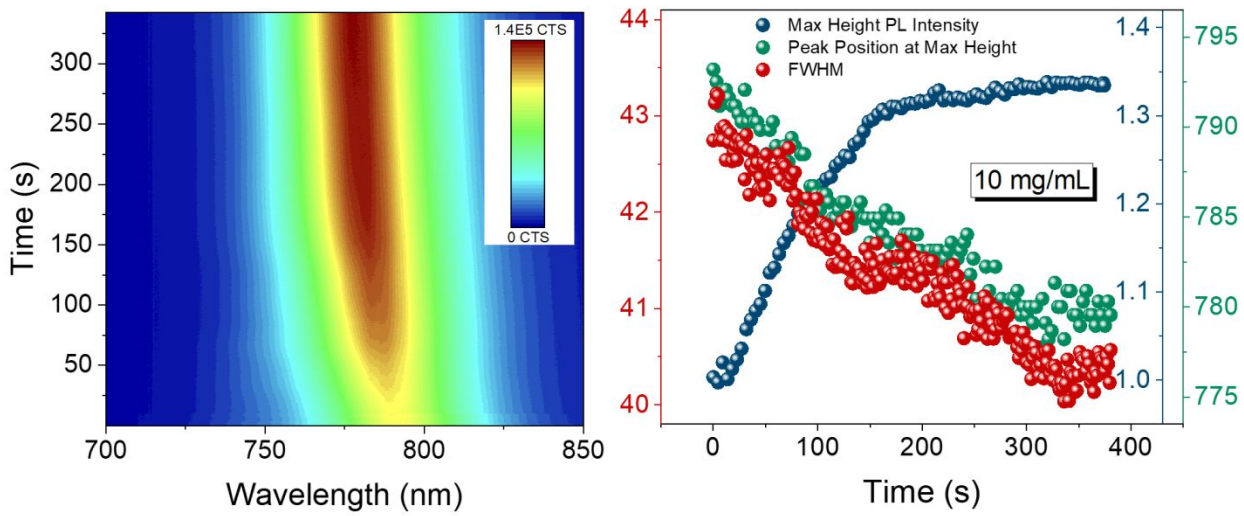

Figure S8. MA^+-FA^+ reaction under PQD concentration of 10 mg/mL. 2D mapping of *in situ* PL evolution (left); 'FWHM', 'max height of PL intensity' and 'peak position at max height' obtained from *in situ* PL data (right)

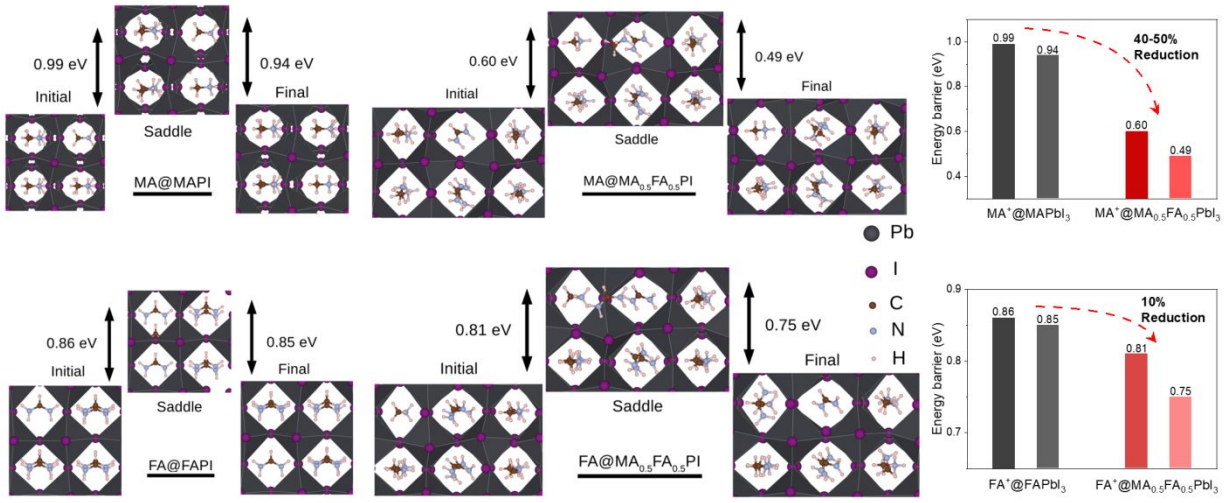

Figure S9. Different configurations (initial-to-saddle, saddle-to-final) under DFT simulation for MA and FA cation diffusion in pure system and mixed system.

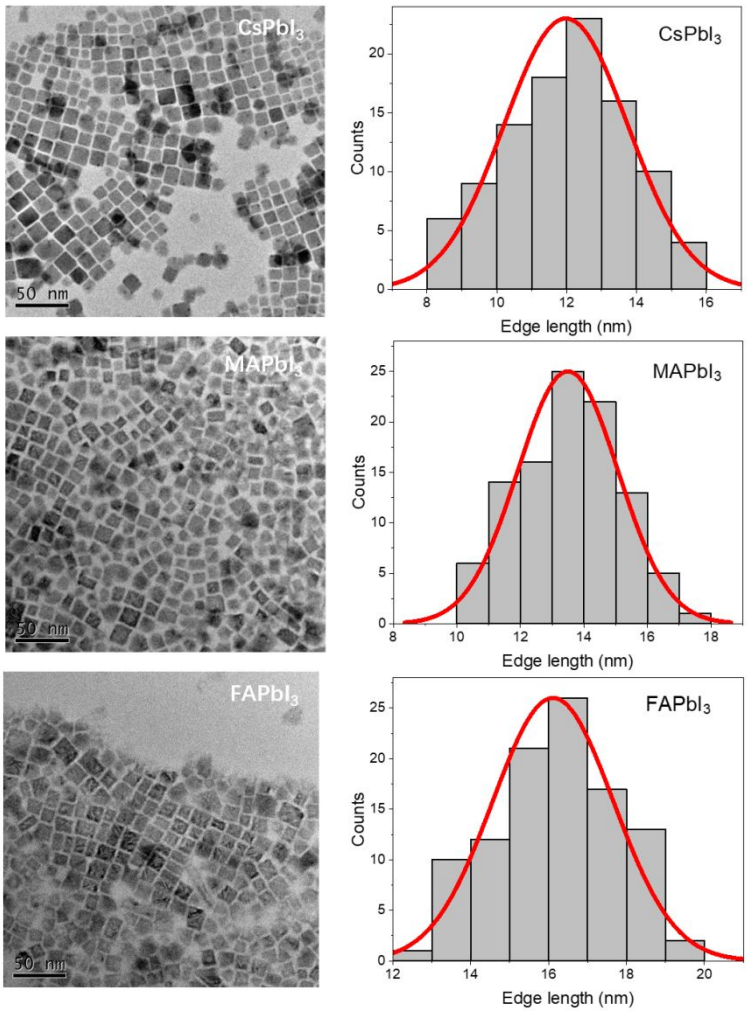

Figure S10. TEM images (left) and size distribution (right) of $CsPbI_3$, $MAPbI_3$ and $FAPbI_3$ PQDs from TEM images

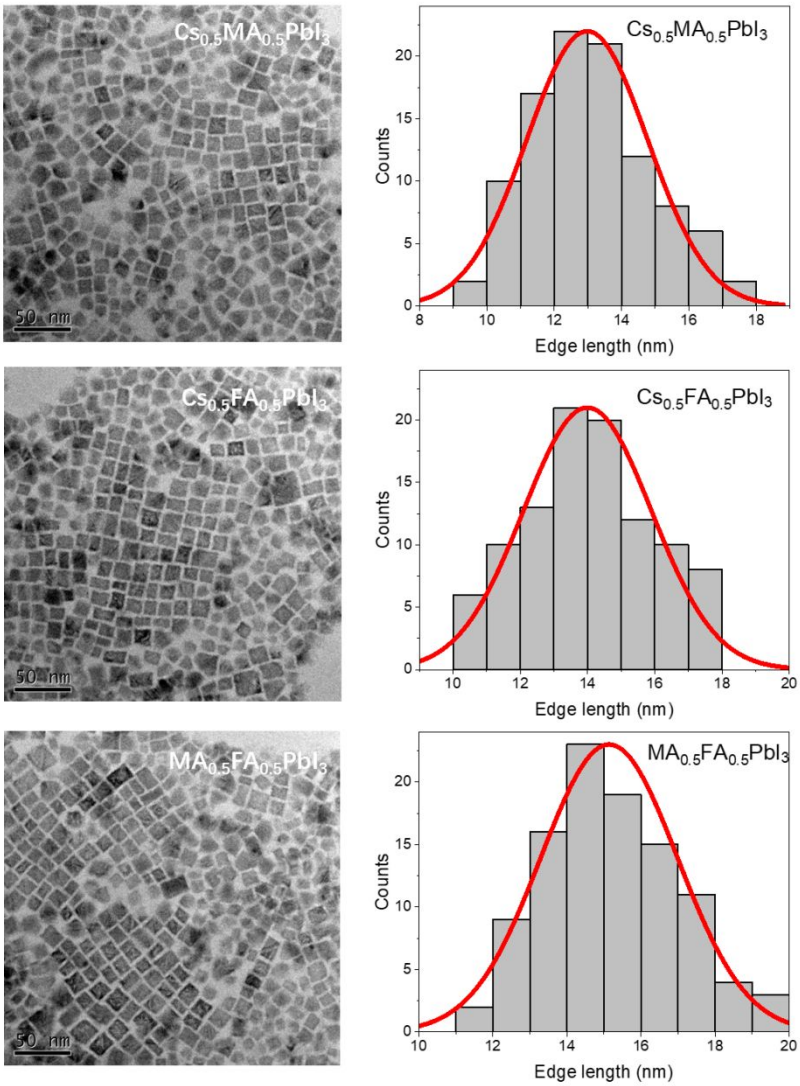

Figure S11. TEM images (left) and size distribution (right) of $Cs_{0.5}MA_{0.5}PbI_3$, $Cs_{0.5}FA_{0.5}PbI_3$ and $MA_{0.5}FA_{0.5}PbI_3$ PQDs

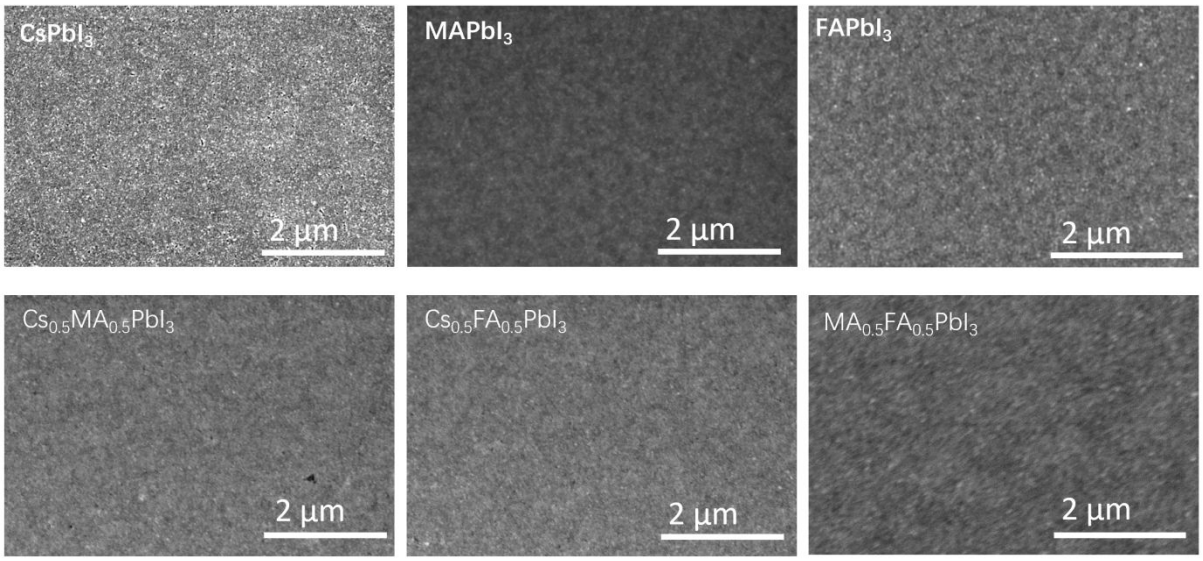

Figure S12. SEM images of $CsPbI_3$, $MAPbI_3$, $FAPbI_3$, $Cs_{0.5}MA_{0.5}PbI_3$, $Cs_{0.5}FA_{0.5}PbI_3$ and $MA_{0.5}FA_{0.5}PbI_3$ PQD films

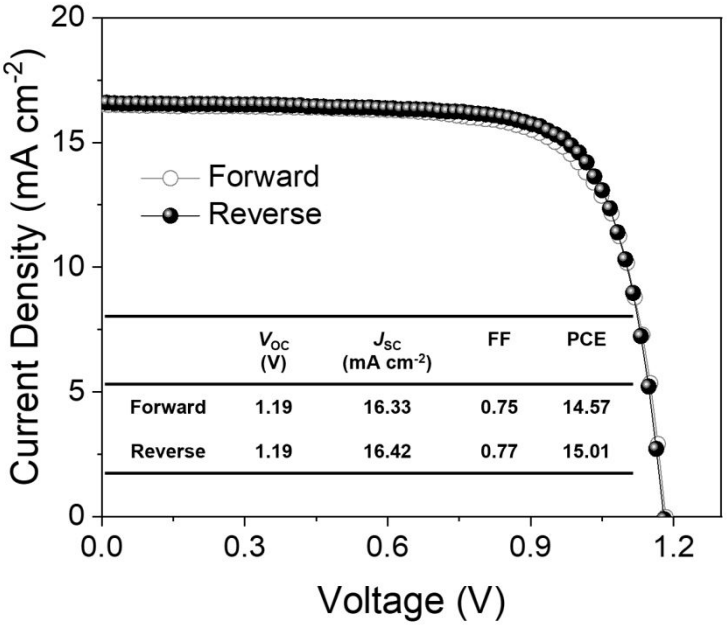

Figure. S13 *J-V* curves under reverse and forward direction for the $MA_{0.5}FA_{0.5}PbI_3$ PQD solar cells

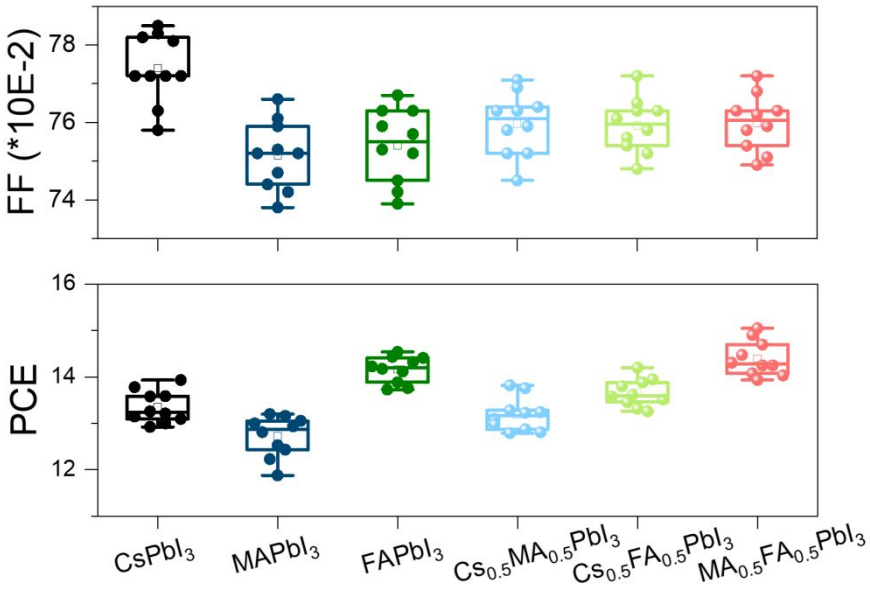

Figure S14. Performance evolution (V_{OC} and FF) of solar cells of different PQD compositions ($CsPbI_3$, $MAPbI_3$, $FAPbI_3$, $Cs_{0.5}MA_{0.5}PbI_3$, $Cs_{0.5}FA_{0.5}PbI_3$ and $MA_{0.5}FA_{0.5}PbI_3$) (10 devices for each composition)

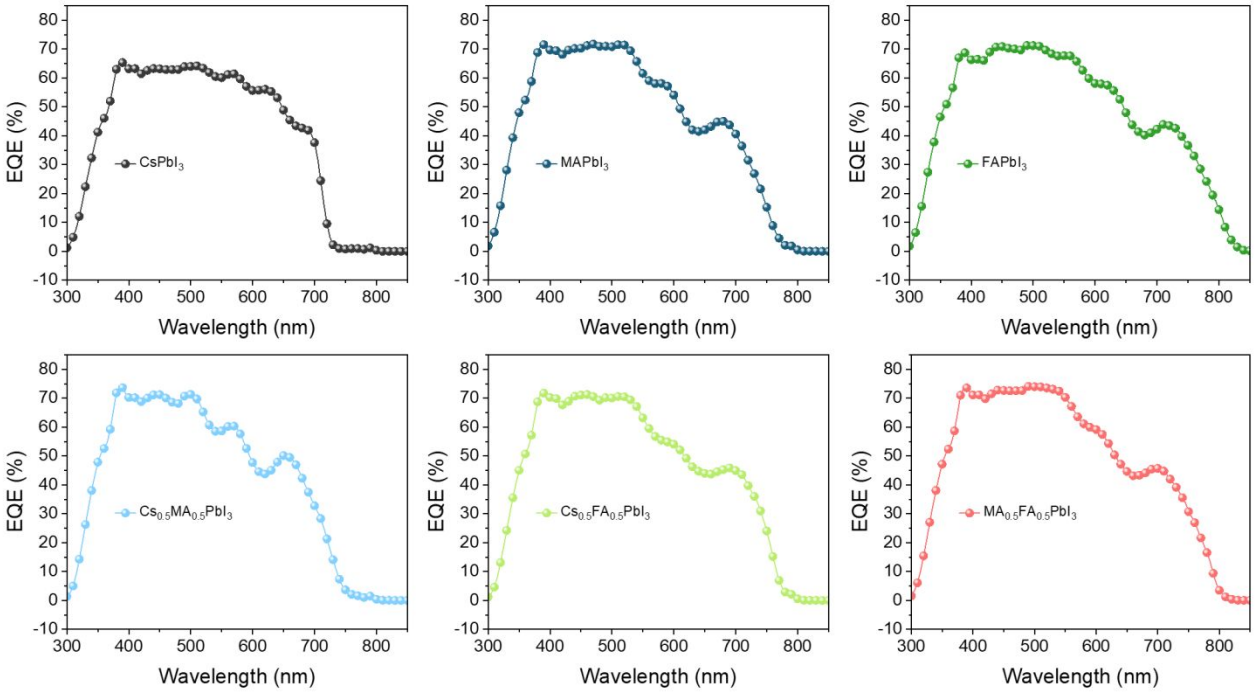

Figure S15. EQE spectrum of different composition ($CsPbI_3$, $MAPbI_3$, $FAPbI_3$, $Cs_{0.5}MA_{0.5}PbI_3$, $Cs_{0.5}FA_{0.5}PbI_3$ and $MA_{0.5}FA_{0.5}PbI_3$) PQD solar cells

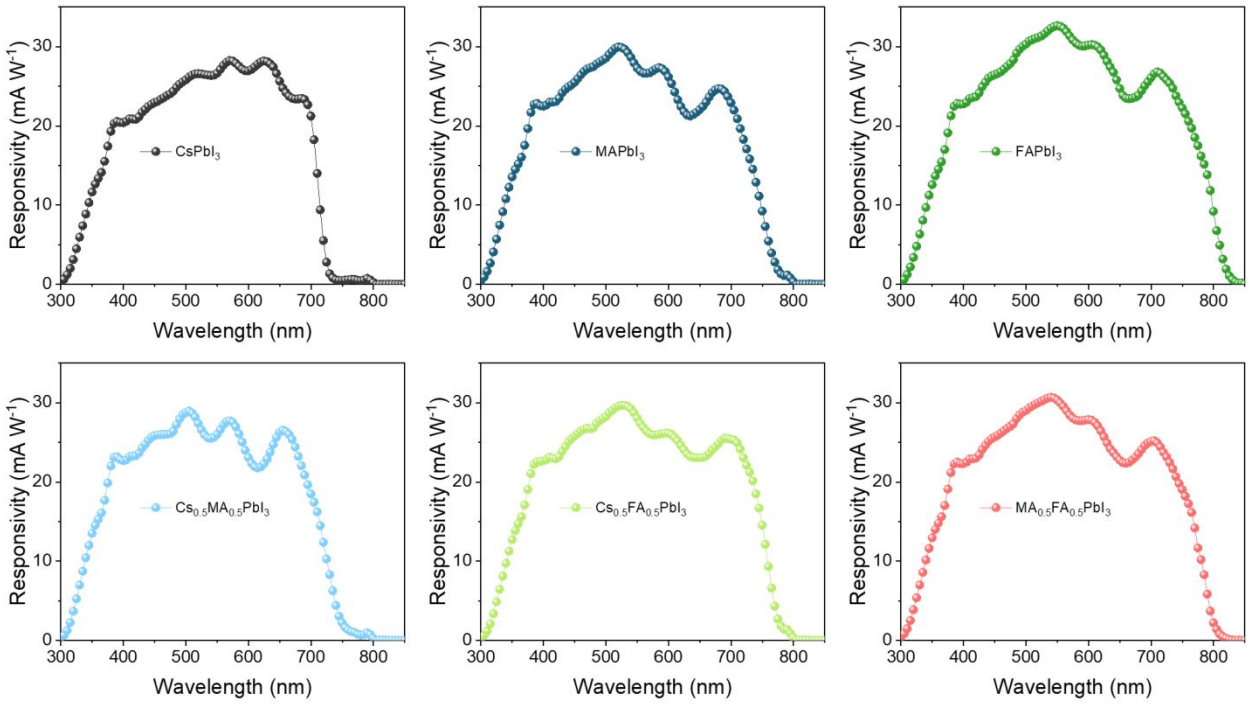

Figure S16. Responsivity of different composition ($CsPbI_3$, $MAPbI_3$, $FAPbI_3$, $Cs_{0.5}MA_{0.5}PbI_3$, $Cs_{0.5}FA_{0.5}PbI_3$ and $MA_{0.5}FA_{0.5}PbI_3$) PQD photodetectors

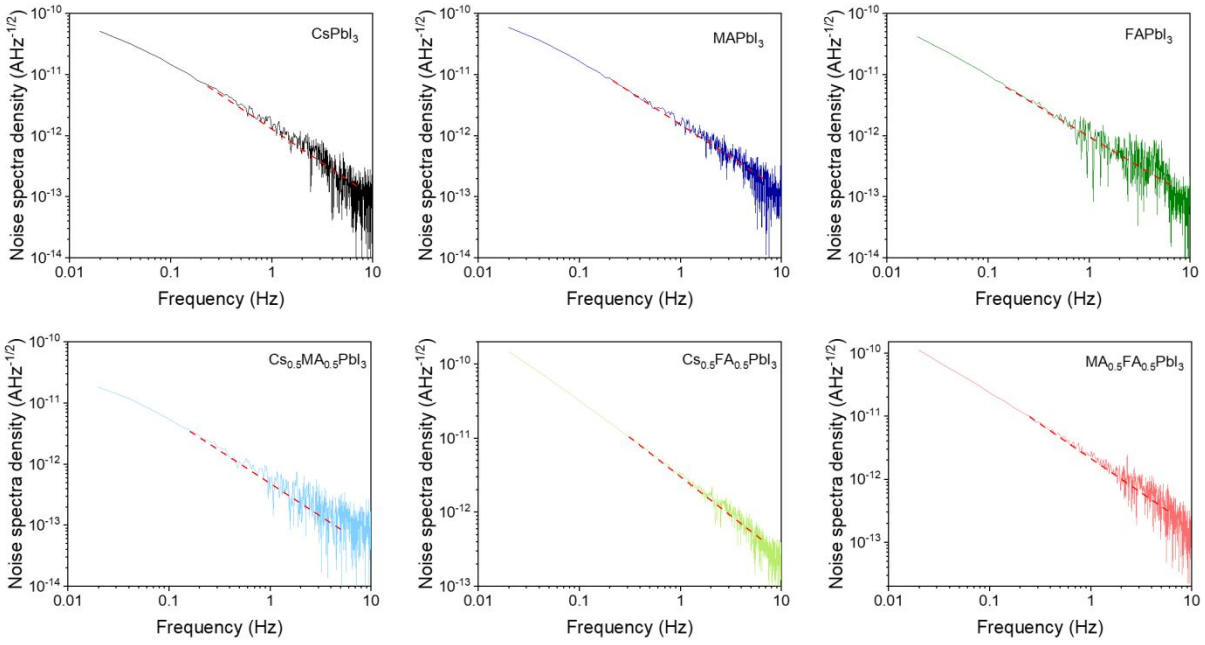

Figure S17. Noise current spectra of different composition ($CsPbI_3$, $MAPbI_3$, $FAPbI_3$, $Cs_{0.5}MA_{0.5}PbI_3$, $Cs_{0.5}FA_{0.5}PbI_3$ and $MA_{0.5}FA_{0.5}PbI_3$) PQD photodetectors

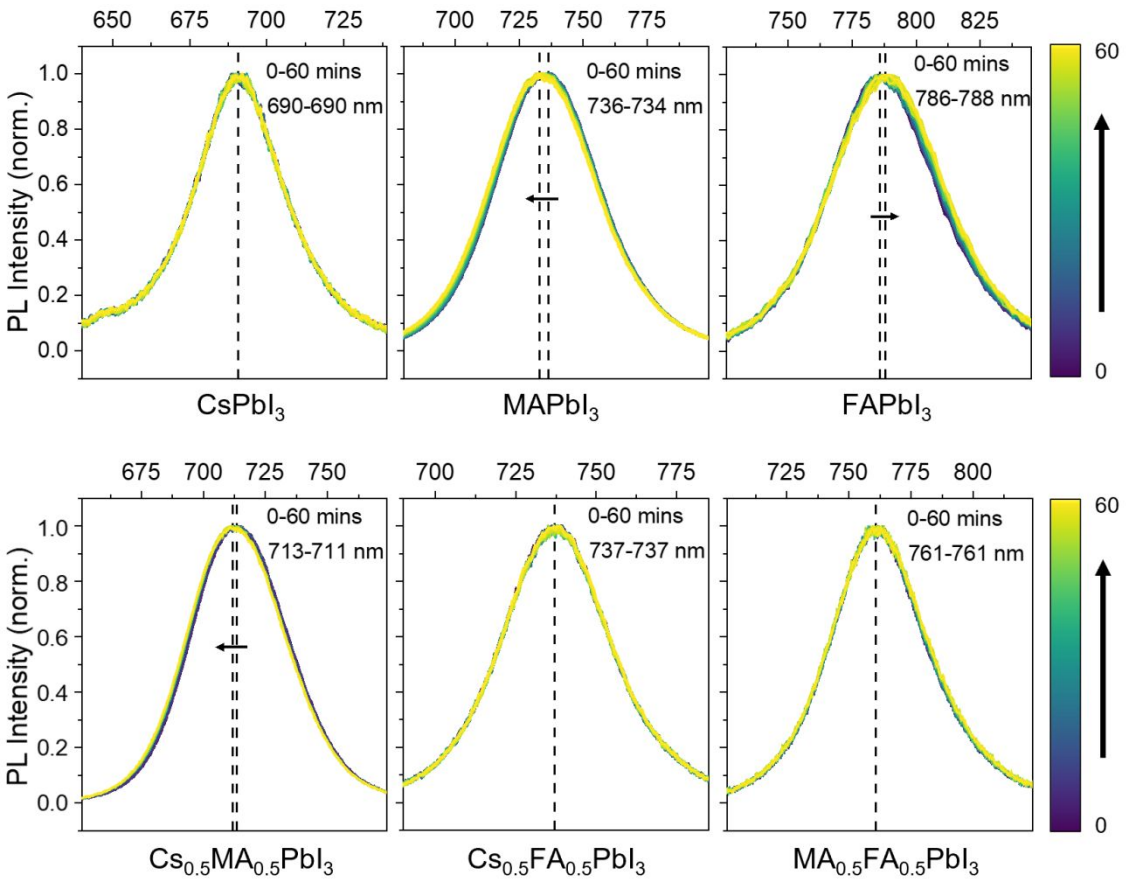

Figure S18. Normalized 1D chart of *in situ* PL spectrum of mixed cation PQD films of $CsPbI_3$, $MAPbI_3$, $FAPbI_3$, $Cs_{0.5}MA_{0.5}PbI_3$, $Cs_{0.5}FA_{0.5}PbI_3$ and $MA_{0.5}FA_{0.5}PbI_3$ after 60 minutes under 100 mW cm^{-2} illumination

Table S1. FWHM fitting of Cs^+-FA^+ cation-exchange reaction

Temperature (°C)	A_1	t_1 (mins)	x_0	k
40	0.119	719.01	4.87	-12.83
50	0.116	390.01	-3.33	-12.17
60	0.120	171.33	-1.36	-11.35
70	0.117	106.78	-0.97	-10.92
80	0.120	53.45	0.54	-10.18

(a) The exchange speed k oriented from the differential of the single exponential fitting: $y = y_o + A_1 * \exp\left(-\frac{x-x_0}{t_1}\right)$, then $k = \frac{A_1}{t_1} * \exp\left(\frac{x_0}{t_1}\right)$.

Table S2. FWHM fitting of Cs^+-MA^+ cation-exchange reaction

Temperature (°C)	A_1	t_1 (mins)	x_0	k
40	0.112	239.66	3.07	-11.80
50	0.109	141.15	1.92	-11.26
60	0.093	75.32	1.53	-10.82
70	0.118	52.87	0.90	-10.11
80	0.134	27.36	0.79	-9.43

Table S3. FWHM fitting of MA^+-FA^+ cation-exchange reaction

Temperature (°C)	A_1	t_1 (s)	x_0	k
40	22.86	190.23	-0.04	-2.12
50	21.58	114.83	-0.01	-1.67
60	22.03	80.28	-0.06	-1.30
70	19.66	55.09	-0.07	-1.03
80	19.25	33.52	-0.03	-0.56

Table S4. *J-V* data of best performance devices

Composition	J_{SC} (mA cm^{-2})	V_{OC} (V)	FF	PCE
$CsPbI_3$	14.47	1.25	0.77	13.93
$MAPbI_3$	14.99	1.19	0.74	13.20
$FAPbI_3$	16.45	1.17	0.75	14.43
$Cs_{0.5}MA_{0.5}PbI_3$	14.84	1.21	0.77	13.82
$Cs_{0.5}FA_{0.5}PbI_3$	15.57	1.20	0.76	14.20
$MA_{0.5}FA_{0.5}PbI_3$	16.42	1.19	0.77	15.05

Table S5. Ion radius and tolerance factor (*t*) (based on $APbI_3$ structure)

Ion	Radius (Å)	*t*
Cs^+	1.80	0.834
MA^+	2.17	0.912
FA^+	2.53	0.987
$(Cs_{0.5}MA_{0.5})^+$	1.99	0.873
$(Cs_{0.5}FA_{0.5})^+$	2.17	0.912
$(MA_{0.5}FA_{0.5})^+$	2.35	0.949

(a) The effective A-site radii for mixed cations are calculated by linear interpolation using the Shannon ionic radii of pure Cs^+, MA^+, FA^+.[7]

(b) Tolerance factors are calculated from the ionic radii of the A^+, Pb^+, I^- ions (r_A, r_{Pb} and r_I) using the equation: $t = \frac{r_A + r_I}{\sqrt{2}(r_{Pb} + r_I)}$, where $r_{Pb} = 1.19$ Å , $r_I = 2.20$ Å.

Reference

(1) Cazorla, C.; Boronat, J. Simulation and Understanding of Atomic and Molecular Quantum Crystals. *Rev. Mod. Phys.* **2017**, *89* (3), 035003. https://doi.org/10.1103/RevModPhys.89.035003.

(2) Perdew, J. P.; Ruzsinszky, A.; Csonka, G. I.; Vydrov, O. A.; Scuseria, G. E.; Constantin, L. A.; Zhou, X.; Burke, K. Restoring the Density-Gradient Expansion for Exchange in Solids and Surfaces. *Phys. Rev. Lett.* **2008**, *100* (13), 136406. https://doi.org/10.1103/PhysRevLett.100.136406.

(3) Kresse, G.; Furthmüller, J. Efficient Iterative Schemes for Ab Initio Total-Energy Calculations Using a Plane-Wave Basis Set. *Phys. Rev. B* **1996**, *54* (16), 11169–11186. https://doi.org/10.1103/PhysRevB.54.11169.

(4) Blöchl, P. E. Projector Augmented-Wave Method. *Phys. Rev. B* **1994**, *50* (24), 17953–17979. https://doi.org/10.1103/PhysRevB.50.17953.

(5) Grimme, S.; Antony, J.; Ehrlich, S.; Krieg, H. A Consistent and Accurate Ab Initio Parametrization of Density Functional Dispersion Correction (DFT-D) for the 94 Elements H-Pu. *The Journal of Chemical Physics* **2010**, *132* (15), 154104. https://doi.org/10.1063/1.3382344.

(6) Zhou, Z.; Chu, D.; Gao, B.; Momma, T.; Tateyama, Y.; Cazorla, C. Tuning the Electronic, Ion Transport, and Stability Properties of Li-Rich Manganese-Based Oxide Materials with Oxide Perovskite Coatings: A First-Principles Computational Study. *ACS Appl. Mater. Interfaces* **2022**, *14* (32), 37009–37018. https://doi.org/10.1021/acsami.2c07560.

(7) Travis, W.; Glover, E. N. K.; Bronstein, H.; Scanlon, D. O.; Palgrave, R. G. On the Application of the Tolerance Factor to Inorganic and Hybrid Halide Perovskites: A Revised System. *Chem. Sci.* **2016**, *7* (7), 4548–4556. https://doi.org/10.1039/C5SC04845A.